manuscript submitted to *AGU Advances*, DOI:10.1002/essoar.10502878.1 (submitted Mar 27, 2020)

The Mysterious Green Streaks Below STEVE

Joshua Semeter[1], Michael Hunnekuhl[2], Elizabeth MacDonald[3], Michael Hirsch[1], Neil Zeller[4], Alexei Chernenkoff[5], and Jun Wang[5]

[1]Department of Electrical and Computer Engineering and Center for Space Physics, Boston University, Boston, MA, USA

[2]Eichenweg 15, 30989 Gehrden, Germany

[3]NASA, Goddard Space Flight Ctr, Greenbelt, MD 20771 USA.

[4]Neil Zeller Photography, Calgary, AB Canada

[5]Alberta Aurora Chasers, Alberta, Canada

Key Points:

- Extremely small point-like features are observed within the 'picket fence' STEVE phenomenon.
- Such features point to the role of local ionospheric production.
- The features are among the smallest optical features found in the natural airglow or aurora.

Corresponding author: Joshua Semeter, Boston University, 8 St. Mary's St., Boston, MA 02215, jls@bu.edu

Abstract

STEVE (Strong Thermal Emission Velocity Enhancement) is an optical phenomenon of the sub-auroral ionosphere arising from extreme ion drift speeds. STEVE consists of two distinct components in true-color imagery: a mauve or whitish arc extended in the magnetic east-west direction, and a region of green emission adjacent to the arc, often structured into quasi-periodic columns aligned with the geomagnetic field (the "picket fence"). This work employs high-resolution imagery by citizen scientists in a critical examination of fine scale features within the green emission region. Of particular interest are narrow "streaks" of emission forming underneath field-aligned picket fence elements in the 100–110-km altitude range. The streaks propagate in curved trajectories with dominant direction toward STEVE from the poleward side. The elongation is along the direction of motion, suggesting a drifting point-like excitation source, with the apparent elongation due to a combination of motion blur and radiative lifetime effects. The cross-sectional dimension is <1 km, and the cases observed have a duration of ∼10–30 s. The uniform coloration of all STEVE green features in these events suggests a common optical spectrum dominated by the oxygen 557.7-nm emission line. The source is most likely direct excitation of ambient oxygen by superthermal electrons generated by ionospheric turbulence induced by the extreme electric fields driving STEVE. Some conjectures about causal connections with overlying field-aligned structures are presented, based on coupling of thermal and gradient-drift instabilities, with analogues to similar dynamics observed from chemical release and ionospheric heating experiments.

1 Introduction

STEVE (Strong Thermal Emission Velocity Enhancement) is a recently identified optical feature in the sub-auroral ionosphere appearing within a narrow channel of extreme westward ion drifts (MacDonald et al., 2018). The phenomenon was identified by citizen scientists using consumer camera equipment. In true-color photography STEVE appears as a diffuse arc extended in the East-West direction with color ranging from mauve to gray-white, which is often, but not always, accompanied by ephemeral green features nicknamed "the picket fence". Multi-point triangulation has placed the mauve component at an altitude range of 130–270 km, with picket fence features extending below to as low as ∼95 km (Archer et al., 2019). Conjugate measurements by the Swarm satellites at ∼400 km altitude have detected $B_\perp$ ion velocities approaching 6 km/s in the STEVE

channel, with evidence for electron temperatures approaching ∼1 eV near the edges (Archer et al., 2019). Initial spectroscopy of STEVE has revealed the mauve color to arise from the oxygen 630-nm red line emission superimposed on a continuum spectrum from ∼400 to ∼700 nm (Gillies et al., 2019). The whitish color is attributed to lower altitude events, where the metastable $O(^1D)$ state responsible for the red line component is collisionally quenched (Liang et al., 2019). The companion picket fence region has been found to be predominently oxygen 557.7-nm green line, with a trace contribution from N_2 first positive emissions (Mende, Harding, & Turner, 2019). The lack of emissions from higher energy N_2^+ transitions has argued against precipitating magnetospheric electrons as a source of the green features (Mende et al., 2019), although the role of precipitation in STEVE remains a subject of debate (Nishimura et al., 2019).

This paper considers STEVE's green companion from a morphological point of view. Particular attention is placed on ephemeral "streaks" of green emission observed below, and conjugate to, field-aligned structures comprising the picket fence. Several examples of this feature are shown in Figure 1, as captured in true-color imagery by citizen scientists. In all cases we have examined thus far, the streaks form on the poleward side of STEVE, exhibit an approximate north-south elongation, and propagate equatorward toward the main STEVE channel. Similar streaks to those shown in Figure 1 are also found embedded in more dynamic displays (e.g., Figure 5), where their motion is somewhat more complicated and their relationship to the magnetic field topology is less clear. Notably, the lifetime of the streaks is sufficiently long (∼10 s) to enable tracking through multiple images, allowing for deconvolution of finite exposure-time effects (motion blur) and spatiotemporal correlation with other features in the field.

In the remainder of this work, we provide an initial examination of the altitude, trajectory, orientation, and dimensions of this feature, followed by some conjectures about its origin, and connections to broader questions of the picket fence source and the modes of energy dissipation represented by the STEVE phenomenon. This work also suggests new opportunities for the use of photometric imaging as a diagnostic of ionospheric turbulence under extreme conditions.

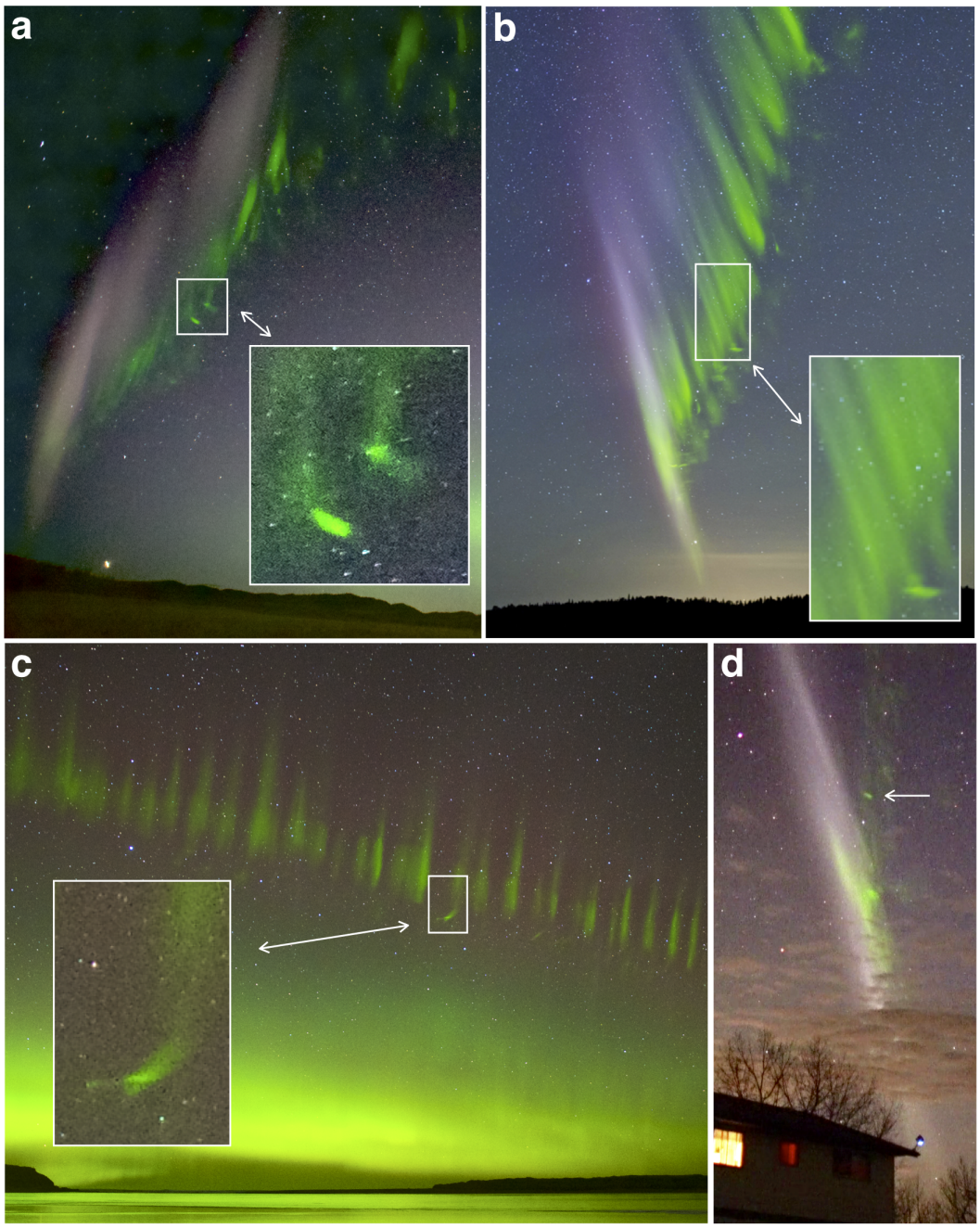

Figure 1. Sample images highlighting STEVE's green component and the mysterious green streaks appearing below the "picket fence" a) 6 May 2018, 11:21:25 LT, 4-s exposure, 51.255°N, 114.701°W (credit: Alexei Chernenkov). b) 13 September 2018, Isle Royale National Park (credit: Shawn Malone). c) 28 March 2017, 15-s exposure (credit: Stephen Voss). d) 6 May 2018, ∼11:19 LT, 33-ms exposure (NTSC video) (credit: Alan Dyer).

2 Analysis results

The experimental results in this work were all derived from imagery recorded by citizen scientists using commercially available equipment. The unfamiliar nature of this phenomenon and the unusual views obtained by the photographers make interpretation with respect to physical hypotheses challenging. Observer perspective, camera exposure times, magnetic field topology, and radiative lifetime effects must all be considered carefully in drawing physical conclusions from these observations. We endeavor to discuss these issues in the context of our analysis. The features of interest are often faint, and the images displayed in this work have been adjusted to enhance contrast. Our findings do not rely on absolute photometric calibration, although that will undoubtedly become an important consideration in future studies.

2.1 Altitude determination

Knowledge of the height of the features provides an important constraint for assessing physical mechanisms. Direct triangulation on the basis of time synchronized images from two locations allows the calculation of the height of aurora, STEVE or airglow structures. Archer et al. (2019) and Palmroth et al. (2019) present algorithms for this purpose in their works. In standard optical triangulation, the position of an object (latitude, longitude, height) is calculated from observer locations and object bearing using standard trigonometric relations. The bearing (elevation and azimuth) of a point in the night sky may be determined with high precision via analysis of the background star field (Lang, Hogg, Mierle, Blanton, & Roweis, 2010). Limiting the analysis to a neighborhood of stars surrounding the features minimizes potential image distortion effects.

Figures 2a and 2b show the images used in our triangulation analysis, recorded from locations (51.255°N, 114.701°W), and (51.267°N, 114.328°W), respectively ((about 50 km WNW of Calgary, Alberta). For the current study, we focus our analysis on the natural triangulation points defined by the leading edge and trailing edge of the streak, labeled R1 and R2. The triangulation geometry is shown to scale in Figure 2c. This triangulation problem exemplifies the opportunities and challenges in using citizen science imagery for precision analyses. The method developed for this study is described in detail in a supporting document, and presented in overview here.

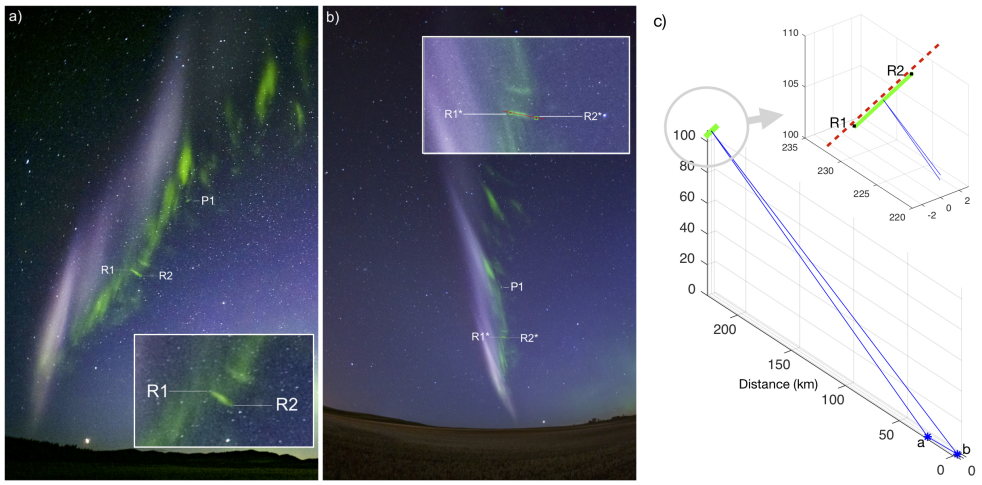

Figure 2. a) Image from the location (51.255°N, 114.701°W) during the same event as Figure 1a. b) Time-synchronized image of the same features recorded from location (51.267°N, 114.328°W) (courtesy Jun Wang). This pair of images was used for triangulation of the low altitude streak with the end points R1 and R2. The altitudes were determined to be 104.6±1.6 km for R1, 106.4±1.6 km for R2.

The images were recorded near 23:20:14 MDT, but the camera time information is unreliable. By analyzing the positions of prominent landmarks on the horizon relative to reference stars in the background, we were able to reconstruct the observation time to within ±2 minutes. The star field is a slowly varying background, and this level of uncertainty translates to a height uncertainty of ∼1 km for objects in the lower ionosphere such as STEVE.

The more significant source of error is the relative time offset between the images. The fine-scale features were changing rapidly in these images. The triangulation result may thus be highly sensitive to small timing errors between images. This is especially true for this geometry (Figure 2c), where the observer separation was small (25.9 km) relative to the target distance (∼230 km). Fortunately, the observer at the location of Figure 2a captured a contiguous time sequence of images of this event. The sequence is shown in Figure 3, highlighting the two prominent streaks in Figure 2. Comparing fine-scale features in the image sequence with features in single frame observation of Figure 2b yielded a near perfect match to the frame displayed in Figure 2a. We conclude that the time offset between the images is <2 s.

Image synchronization is further improved through the use of a modified triangulation method that exploits the unique one-dimensional geometry of these features. The streaks in Figure 3 are seen to move along a line corresponding to their direction of elongation (the significance of this is further discussed in Section 2.2). We therefore assume the streaks were moving in a straight line through three-dimensional space during the exposure, and that the images represent two-dimensional projections of this line (i.e., an affine transformation). We next let R1 and R2 in Figure 2a be fixed reference points. The projections of these points in Figure 2b are unknown, but they are assumed to lie along a line defined by the streak (depicted in red in Figures 2b (inset) and Figure 2c). The geophysical coordinates of points R1 and R2 were found by testing points along the red line for consistency with both projections. Specifically, for each test point the position of the ground intersection was computed from the elevation and azimuth information, and the corresponding altitude was computed independently for each observer. The solution is the position at which the altitudes agree. The logic of the method is that there is only one line in 3D space that is consistent with a line in 2D space observed from two locations.

The optimal positions of R1 and R2 in Figure 2b are labeled R1* and R2*. It is interesting to note that R1 and R1* both lie on the leading edge of the streak in their respective images, where the edge is well defined, while R2* lies a bit behind the trailing edge, which is somewhat broader and more diffuse. For R1 the optimized mean height is 104.6 m ±1.6 km, and for R2 it is 106.4 km±1.6 km. Uncertainties were estimated using a Monte Carlo method. Histograms of triangulated heights were constructed based on 10,000 trials distributed uniformly over the range of pointing uncertainties defined

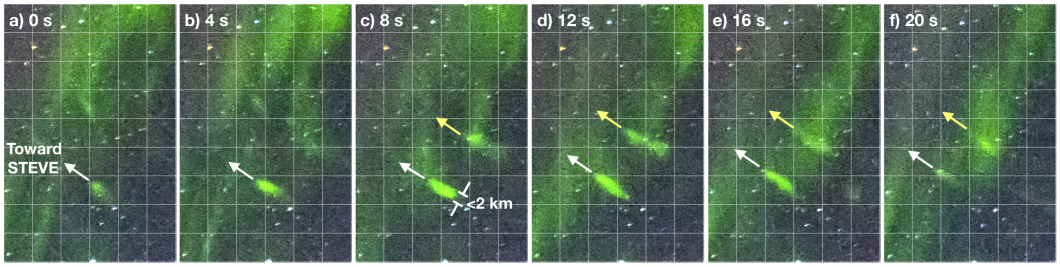

Figure 3. Sequence of 4-second image samples around the time of Figure 1a, showing the general propagation of the streaks toward the main STEVE arc, and their general elongation in the direction of propagation.

by uncertainties in timing, feature dimensions, and observer location (minor). The uncertainty ranges reported above are the interdecile ranges of the resulting histograms. Further detail is presented in the supplemental document.

We conclude that the streak R1–R2 resides in the lower ionospheric E-region in the altitude range of 100–108 km, with some evidence for a slight downward orientation of the streak toward the main STEVE arc. This is consistent with observations of trajectories in other events, as discussed in Section 2.2 and 3.3.

2.2 Trajectory

Figure 3 shows a sequence of cropped images at 4-second cadence, documenting the formation and evolution of the two streaks highlighted in Figure 1a and 2a. The streaks initially appeared as point-like features (white arrow in panel a, yellow arrow in panel c), which subsequently elongate along their direction of motion. The trajectory has a dominant component toward the the main STEVE channel in these observations. The elongation of the features is influenced by at least three effects. The first is simple motion blur caused by the 4-s exposure. The second is emission afterglow. As suggested in prior work (Gillies et al., 2019; Mende et al., 2019), the green color is predominantly due to the 557.7 nm line, produced by the metastable $O(^1S{-}^3P)$ transmission of atomic oxygen, with radiative lifetime 0.74 s. A moving source of $O(^1S)$ will produce a luminous tail in the 557.7-nm emission due to the finite radiative lifetime. The third effect is spatiotemporal variability in the excitation source itself.

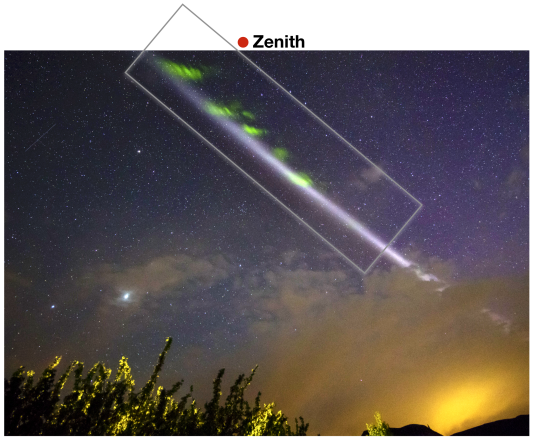

Figure 4. STEVE observed with 15-second exposure on 00:33:22 LT on 20 March 2017 from location 51.66 N, 112.91 W. The rectangle is the region detailed at 3.5-second exposure in the image sequence of Figure 5 (courtesy Neil Zeller Photography).

The streaks appear with with a wide range of contrast in the image sequences examined thus far (e.g., Figure 1a is a 4-s exposure, while Figure 2d is a 40-ms exposure). From the evidence acquired thus far, it is difficult to assign differences in apparent streak brightness to equipment disparities versus differences in source brightness. In order to better quantify the effects described above, we turn to an event that was far more dynamic while also exhibiting greater dynamic range in the image sensor.

Figure 4 was recorded on 20 May 2017 at 00:32 Local Time (LT) from location 51.66 N, 112.91 W at 15-second exposure. In this display, a series of coherent green structures are observed to extend away from the main STEVE channel. The two structures toward the top of the image are composed of periodically spaced bands, each aligned approximately parallel to the main STEVE channel. The local vertical zenith direction lies just outside the field of view, as indicated by the red circle. The mauve-white arc is stretched out along the magnetic east-west direction. The orientation of the green features in Figure 4 is difficult to establish in this projection. Accounting for the geometric point of view is particularly important in the under-studied sub-auroral region, where the field lines are not vertical, and the features are not easily reconciled with intuition developed from auroral observations.

This event was captured by a second co-located camera with narrower field of view and higher image cadence (3.5-second). Figure 5 shows four selected images from this

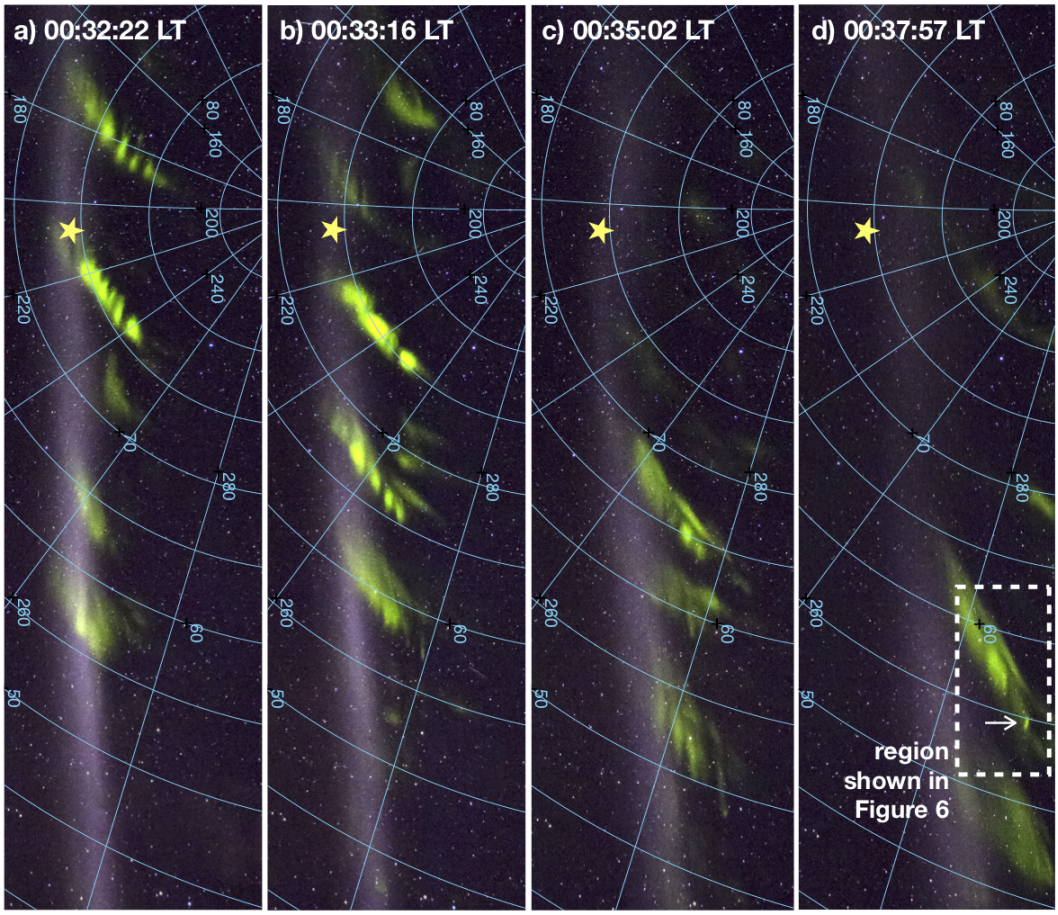

Figure 5. Sample images of dynamic green emissions observed within the rectangular region of Figure 4. Azimuth and elevation contours are shown in blue. The magnetic zenith direction is indicated by the yellow star.

camera, with local time as indicated. The field-of-view corresponds to the rectangular region in Figure 4. Blue contours indicate geographic azimuth and elevation as determined from star field fitting using the Astrometry.net package (Lang et al., 2010). The yellow star in each frame indicates the magnetic zenith direction (inclination 73.5°, declination 14°), calculated using the International Geomagnetic Reference Field (IGRF) model (Thébault et al., 2015))

The image samples in Figure 5 were selected to give a sense of how these features varied as they moved westward from near zenith (panel a) to lower elevation (panel d). The individual features changed substantially from frame to frame, indicating that this phenomenon was not fully resolved at 3.5-seconds. Dynamic features in the high-latitude

aurora exhibit orientations and motion that are clearly organized with respect to the magnetic field, with the local magnetic zenith serving as the point of convergence (e.g., Dahlgren, Semeter, Marshall, & Zettergren, 2013). The features in Figure 5 exhibit no definitive or stable orientation with respect to the magnetic field. The reader is encouraged to view the full image sequence included as supporting information in time-lapse format (movie MS3).

One feature that remained coherent across multiple frames is the small streak within the dashed box of Figure 5d. This streak has characteristics similar to the streaks in Figures 1 and 3 – i.e., it is the smallest object within the field, it appears below the other features (i.e., lower elevation), and, unlike other features in this sequence, it persisted as a coherent drifting object across several frames.

Figure 6a-e shows the evolution of this feature through five consecutive 3.5-second frames. The field-of-view corresponds to the dashed box in Figure 5d. Figure 6f duplicates the image of Figure 6e with fiducial marks inserted: the white arrows show the location, length, and direction-of-motion of the streak as extracted from each of panels a–e. The streak is seen to be contiguous from frame to frame (i.e., tip of one arrow lines up with tail of the next). This suggests that it is produced by a drifting point-like source, and that the observed elongation is primarily caused by motion blur and afterglow effects previously discussed. The trajectory is also seen to be slightly curved in this perspective. The curvature is consistent with bending toward the main STEVE channel. This trajectory may have similarities to Figure 1c, where the trace emission behind the streak suggests a drift path that bent into the horizontal plane. The red line inserted in panel f indicates the magnetic field-aligned direction. Its significance will be discussed in Section 2.3.

2.3 Dimensions and Velocity

The high fidelity of Figure 6 allows for a quantitative examination of dimensions and velocities of the streak. Figure 7 shows the relative brightness of the camera's green channel versus distance along its trajectory for each panel (a–e) of Figure 6. The distance scale was computed in the following manner. First, the plate scale, $p = 0.0257$ radians/pixel, was determined for the region of interest (Figure 5d, inset) using the star field calibration. Next we select as the origin a pixel (x_0, y_0) corresponding to the tail

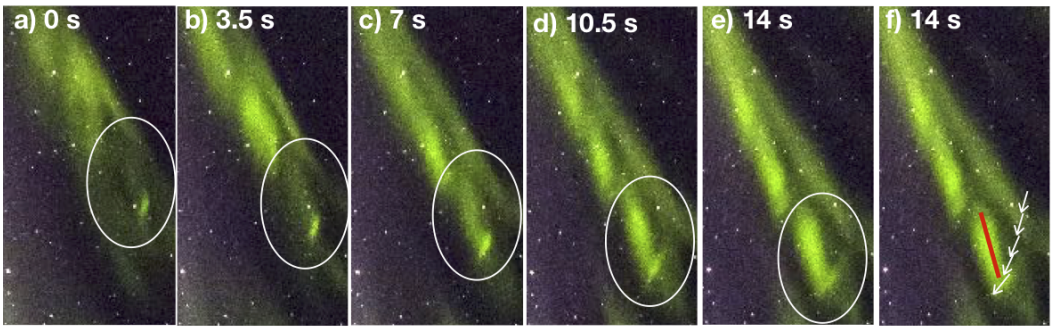

Figure 6. Image sequence at 3.5-second cadence corresponding to the rectangular region in Figure 5d, showing the evolution of an emission streak that persisted in 5 contiguous frames (feature within the white oval). In panel f, the length, orientation, and direction of motion of the streak is shown as a series of vectors. The red line shows the magnetic field-aligned direction superimposed on a features that formed above the streak.

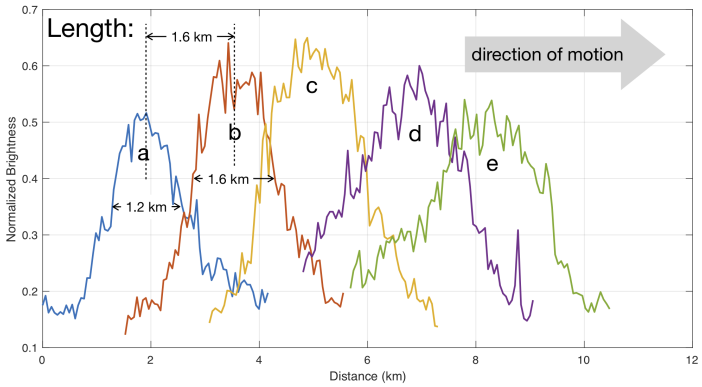

Figure 7. Normalized brightness as a function of distance along the trajectory of the streak feature in Figure 6a-e. The behavior is consistent with a drifting point source. An asymmetry develops as the object moves, consistent with an "afterglow" tail due to the 0.74-s radiative lifetime of the $O(^1S)$ state.

of the first arrow in Figure 6f. The selection of this point is somewhat arbitrary, as it is the relative motion between frames that is of interest. The range to this point is given by $R_0 = z_0/\sin(\theta_0)$, where θ_0 is the elevation and z_0 is an assumed feature altitude, taken to be 100 km. The pixel coordinates (x_p, y_p) of a cut through the feature are then converted to physical distance d using the small angle formula,

$$d = R_0 p\sqrt{(x_p - x_0)^2 + (y_p - y_0)^2} \quad \text{(km)}. \tag{1}$$

The streak trajectory through three-dimensional space is unknown. The distance scale so derived corresponds to a projection of the actual distance scale into the image plane under the stated assumptions. If we assume a point-like object that elongates in the direction of motion, this scale approximates the projected distance in km along the trajectory traced by the white arrows in Figure 6f. At its initial appearance, the full-width-at-half-maximum (FWHM) is similar to the separation between peaks. This result is consistent with a moving point source subject to motion blur. The streak can also be seen to broaden and develop an asymmetric "tail" behind its trajectory. This is qualitatively consistent with the afterglow effect due to the finite radiative lifetime of the $O(^1S)$ state. If the actual trajectory has a component orthogonal to the image plane, the widths and peak positions extracted from Figure 7 would be compressed by a common scale factor.

Figure 8 shows the evolution of this feature in the direction *transverse* to its propagation. The curves have been manually shifted to align the lower altitude edge of the streaks, in order to compare relative changes in width during its lifetime. When first observed (curve a) the streak has a cross-sectional width of ∼350 m. This streak is thus among the smallest optical aeronomical features observed at any latitude in the aurora or airglow. As it evolves through subsequent frames (curves b–e), an extended region of emission is seen to develop to the left (i.e., at higher elevation angle). Some context for this can be obtained by returning to Figure 6. The new region of emission corresponds to a developing magnetic field-aligned feature in the upper part of the encircled region, above the streak. In Figure 6f, a red bar has been inserted to show the magnetic field-line direction projected into the image plane. Magnetic conjugacy of low-altitude streaks and field-aligned features is also observed in the wide-field image samples of Figure 1. The analysis of Figure 8 provides possible evidence for the contemporaneous development of the low altitude streaks of emission and magnetic field-aligned features above it.

3 Discussion

True-color images of selected STEVE events obtained by citizen scientists have been used in a critical examination of small-scale features in the green "picket fence" region. Image sequences acquired at 3.5- and 4-second cadence have revealed dynamic sub-kilometer features with varying orientations, dimensions, and motions (Figures 5 and 6). Unlike

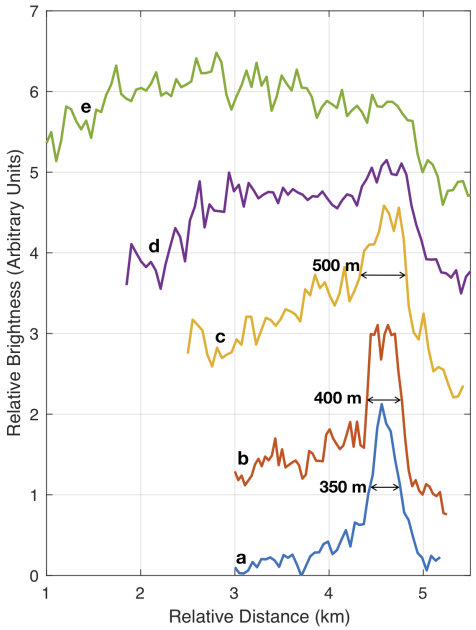

Figure 8. Brightness cuts extracted through the highlighted feature in panels a-e of Figure 6 in a direction aligned with the magnetic field, showing as a line plot the apparent field-aligned elongation of the structure during its lifetime.

the quasi-periodically spaced green columns that inspired the "picket fence" designation, these features are not extended along magnetic field lines, and are thus inconsistent with production via energetic particle precipitation. Readers are encouraged to view the three time-lapse videos included as supplemental material in order to develop their own impression of these unusual features, and the unique perspectives obtained by citizen scientists.

This work has focused on a particular repeatable feature: a narrow "streak" of emission appearing below the picket fence that propagates toward STEVE from the poleward side. This feature is noteworthy for several reasons: 1) it is the lowest-altitude and smallest-scale optical feature associated with STEVE, 2) it has been observed in many STEVE events (Figure 1), 3) in events where contiguous image sequences are available, the feature has been observed to persist for >10 s as a coherent propagating object (Figure 3, Figure 6, and supporting videos), 4) it is magnetically conjugate to, and sometimes optically connected with, overlying field-aligned structures. The following sections present some conjectures based on the initial analysis reported herein.

3.1 Source of green line excitation

The periodic spacing and magnetic field elongation often observed in the green features adjacent to STEVE (e.g., Figure 1) have naturally led many to assume production via usual auroral mechanisms – i.e., penetration of magnetospheric electrons with kinetic energy >1 keV (e.g., Gillies et al., 2019; Mishin & Streltsov, 2019; Nishimura et al., 2019). The initial spectroscopic measurements acquired by Gillies et al. (2019) are irreconcilable with this hypothesis. A careful analysis by (Mende et al., 2019) found the spectrum to be dominated by the metastable oxygen 557.7-nm line (4.19 eV excitation energy, 0.74-s radiative lifetime) but with a trace contribution from prompt N_2 first positive (1P) emissions (7.35 eV excitation energy). Entirely absent, however, were contributions from higher energy emissions of N_2^+, often represented in auroral studies by the band-head of the the N_2^+ first negative (1N) group at 427.8 nm (18.75 eV excitation energy). This emission, produced by collisional ionization and excitation of ambient N_2, must be present for particle penetration to these altitudes. The presence of N_2 1P without N_2^+ 1N has argued for a lack of primary electrons with the requisite >1-keV energy range, rather than a depletion of ambient N_2 (Mende et al., 2019). This finding supported earlier conjectures based on color comparisons (Mende et al., 2019) that the source of the green companion to STEVE is likely direct excitation of oxygen $O(^1S)$ by superthermal electrons energized locally in the ionosphere.

For the features examined in this work, the particle precipitation hypothesis is excluded based on more direct morphological considerations. The small scales and variegated orientations of the lower ionospheric features highlighted in Figures 1–6 cannot be accounted for by energetic electron penetration. Analysis of the streak in Figures 6 and 8 are consistent with a drifting point-like source, with cross-sectional size as small as ∼350 meters. Triangulation of a similar feature in Figure 2 has placed this source in the lower ionospheric E-region in the 100–110 km range, and below other picket fence features in the field.

3.2 Superthermal electron production

In seeking a local source of free energy able to excite oxygen green line features at sub-kilometer scales, it should be noted that the ion drift speeds within STEVE exceed 6 km/s (Archer et al., 2019; MacDonald et al., 2018). The patterns and intensities of tur-

bulent heating caused by such supersonic plasma jets in the outer atmosphere are not well known. Additional complexity arises from the entanglement of chemistry and electrodynamics: ion velocities in this range are known be associated with rapid conversion from atomic (O^+) to molecular (NO^+) ions (Anderson, Heelis, & Hanson, 1991), which would impact momentum balance in the channel in a highly nonlinear manner. Under these conditions it is not surprising to find pockets of extreme electron heating.

Some evidence for this has been found in conjugate satellite measurements. Nishimura et al. (2019) and Archer et al. (2019) have reported measurements from the SWARM satellites of a narrow channel of electron heating conjugate to STEVE, with T_e exceeding 8,000 K, as well as a single-point measurement approaching 12,000 K (>1 eV). These measurements occurred in a region of depleted plasma densities and large upward ion velocities, consistent with expected signatures of low-altitude heating. The measured electrons are certainly non-thermal, but a distribution with average energy ∼1-eV would be expected to include a significant population at the requisite 4.19 eV energy for green-line excitation. Candidate mechanisms for superthermal electron production in the low-altitude ionosphere include the modified two-stream (Farley-Buneman) instability (Farley, 1963; Oppenheim & Dimant, 2013), and the electron and ion thermal instabilities (Dimant & Sudan, 1997). These instabilities have the lowest threshold in the 100 to 120 km altitude range (Dimant & Oppenheim, 2004), which is consistent with the altitude range found via triangulation in Section 2.1. The kilometer cross-sectional dimensions found in Section 2.3 are consistent with scale sizes of irregularities produced in simulations (Oppenheim & Dimant, 2013). Electron temperatures as high as 6000 K have been observed in associated with plasma heating by Farley-Buneman waves (Bahcivan & Cosgrove, 2010). Using the linear relationship of (Foster & Erickson, 2000), this would correspond to an electric field of ∼300 mV/m which, in turn, corresponds to ion drits of ∼6 km/s. It is quite likely that the STEVE parameter set is even more extreme.

The manifestation of these turbulent processes in airglow or auroral signatures has not been fully considered. The hypothesized photochemical model for the production of the 557.7-nm emission is

$$O(^3P) + e(E) \quad \longrightarrow \quad O(^1S) + e(E - 4.19\text{eV}) \tag{2}$$

$$O(^1S) \quad \longrightarrow \quad O(^3P) + h\nu_{557.7} \tag{3}$$

(Itikawa & Ichimura, 1990). (We note that the $O(^1D)$ state, responsible for the oxygen 630-nm redline, is excited through the same collisional reaction but at lower energy (1.96 eV). However, it is quenched at lower ionospheric altitudes due to its long (∼120-s) radiative lifetime). Extracting spatiotemporal information about electron heating from images of this emission requires careful consideration of source dynamics and radiative lifetime effects, as represented in the space-time perspective of the sensor. It must also be borne in mind that the images only provide information about electrons with energy >4.19 eV (45,0000 K). Lower energy superthermal populations are important and presumably present, but invisible in green-line imagery. A full treatment of these effects is beyond the scope of this work. But a qualitative appreciation of these effects is useful in the evaluation of evidence from citizen science imagery.

3.3 Relation to magnetic field-aligned features

An initial examination of image sequences has provided evidence for connections between the low altitude emission streaks, and magnetic field-aligned features comprising the "picket fence." The evidence is summarized in Figure 9 for the examples of this study. In each panel, the grayscale image depicts the green channel of the camera, displayed as a negative for ease of annotation. The red arrows highlight features aligned with the magnetic field; the blue arrows indicate the orientation and trajectory of the streaks. Figure 9a corresponds to Figure 3c. At this point in time, the upper streak has developed a visible tail extending behind the trailing edge, which is qualitatively consistent with the afterglow effects discussed in Section 2.2. This streak also exhibits a faint emission column extending above it in the magnetic field-aligned direction. The combination of these effects form an intriguing "L" shape in the image.

Figure 9b is from Figure 1b. Multiple horizontal streaks can be seen conjugate to field-aligned aurora-like structures. Panels c and d provide some supporting evidence for this conjecture. Panel c (from Figure 1c) shows evidence of a curved tail behind the feature, which bends from the field-parallel direction into the horizontal direction at lower altitudes. If the green line is excited by a drifting source of hot electrons, then the drift would be confined to the $B_{\parallel}$ direction at higher altitudes, but develop an increasing $B_{\perp}$ component at lower altitudes, where increasing electron-neutral collisions lead to increasing cross-field mobility, allowing electrons to respond directly to the poleward directed electric field of the sub-auroral ion drift (SAID) channel.

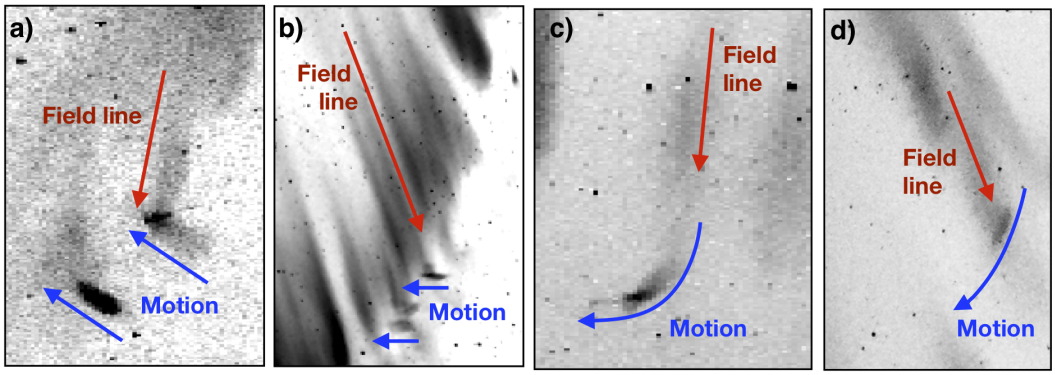

Figure 9. Relationship between magnetic field-aligned features (red), streak orientation, and streak motion (blue) for examples used in this study. The images show the green channel of the cameras, displayed as a negative (emissions are dark) a) From Figures 1a and 3c. Blue arrows show the horizontal equatorward direction of motion, as observed in Figures 3a-f. b) From Figure 1b. Blue arrows show the orientation of the streaks in relation to magnetic field direction. c) From Figure 1c. The blue curve highlights the curved shape of the airglow feature which appears to bend into the field-perpendicular equatorward direction. d) From Figure 5g (rotated 90°). Blue curve shows the complete trajectory as extracted from the image sequence in Figures 5e-j.

This interpretation is speculative based on a single still image. However, a similarly curved trajectory was observed in Figure 9d. The blue curve corresponds to the collection of arrows in Figure 6f, which track the trajectory through Figures 6a-e. The temporal development of a magnetic field-aligned feature above the streak was similarly observed in these frames. This process was summarized in Figure 8, where the cross-sectional width of the streak began with a value of ∼350 m (curve a). As the streak drifted, the emission was observed to extend upward in the magnetic field-aligned direction.

Our triangulation analysis has placed the altitude of the streak in the lower ionospheric *E*-region (100–110 km), where neutral collisions become an important consideration in plasma transport. The aggregate evidence in Figure 9 suggest a propagation path that bends into the horizontal plane as altitude decreases. This observation is qualitatively consistent with expected effects in this altitude range.

3.4 Formation of field-aligned features from point sources

One question that arises naturally from the evidence assembled thus far is whether field-aligned "aurora-like" optical features can evolve from point-like sources created through turbulent heating. Preferential expansion of an isolated plasma population along the magnetic field direction is expected considering the difference in field-parallel versus field-perpendicular mobility (Rishbeth & Garriott, 1969). A possible structuring mechanism lies in the coupling between Farley-Buneman and gradient-drift instabilities, which arise from a common dispersion relation (Fejer & Kelley, 1980). The coupling effects can be amplified in regions of extreme density gradients (Haldoupis, Ogawa, Schlegel, Koehler, & Ono, 2005), such as those found on the poleward edge of an extreme SAID channel.

The evolution of cloud-like features into aurora-like features has been well documented in artificial plasma release experiments (Haerendel & Lüst, 1968), where a cloud of ionized Barium (Ba^+) is observed to rapidly striate across magnetic field lines and elongate along magnetic field lines, forming structures reminiscent of rayed aurora within a few seconds (Simons, Pongratz, & Gary, 1980). The cross-field striation is thought to be caused by the gradient drift instability (Linson & Workman, 1970; Simons et al., 1980). This mechanism is also plausible here due to the presence of extreme electric fields and extreme density gradients on the edges of the STEVE channel (Nishimura et al., 2019).

In chemical release experiments, the injected plasma was a cold long-lived Barium ion (Ba^+) illuminated by sunlight fluorescence. In the present situation, the illuminating agent would be superthermal electrons with energy >4.19 eV exciting the oxygen $O(^1S)$ state. In the image sequences of Figures 3 and 6, the excitation source persisted for >10 s, which is long compared with time scales for field-line elongation observed in Barium releases (Simons et al., 1980).

However, based on the limited evidence thus far obtained, it is also possible that the streaks and the picket fence are not causally connected but, rather, represent two distinct responses to the same free energy source. Mende et al. (2019) conjectured that the magnetic field-aligned features could be produced by wave heating induced by the extreme electric fields in the SAID region (Streltsov & Mishin, 2003). Fine-scale green emissions at lower conjugate altitudes could be excited by these same extreme fields.

4 Conclusions

Thus far, nothing about the optical phenomenology associated with STEVE is conveniently explained in terms of our historical understanding of auroras and airglow (Gillies et al., 2019; Harding, Mende, Triplett, & Wu, 2020; Mende et al., 2019). The reason for this may be generally traced to the extreme nature of the driving electric fields and attendant supersonic ion drifts. This regime of ion-neutral interaction has not been systematically treated in aeronomical models. The mauve-white emission of the main STEVE channel is likely related to the continuum nightglow emission that has been known for decades Bates (1993). Our understanding of its origin remains incomplete, but STEVE has attracted renewed attention to the topic (Harding et al., 2020). The green features accompanying STEVE often exhibit elongation in the magnetic field direction, suggesting they are produced by precipitation of magnetospheric electrons (Nishimura et al., 2010). But initial spectroscopic measurements are inconsistent with this hypothesis (Mende et al., 2019). The green phenomena accompanying STEVE also include a variety of blobs, streaks, and curved bands of emission (Figure 5), that are irreconcilable with the precipitation hypothesis on morphological grounds alone.

This work has focused on a particular repeatable feature of the STEVE green-line phenomenology: a narrow streak of emission observed below, and connected with, the field-aligned features comprising the picket fence. An initial analysis has been presented using time-lapse imagery and multi-station observation, revealing the following characteristics.

1. Formation is poleward of STEVE and in the lower ionosphere (100–110 km).
2. Movement follows a curved trajectory, with dominant component toward the main STEVE arc.
3. Elongation is along the direction of motion, suggestive of an unresolved moving point source.
4. Lifetime of an individual streak is ∼10–30 s,
5. Location is conjugate to, and sometimes optically connected with, field-aligned features above it.
6. Cross-sectional dimension is <1 km and thus irreconcilable with production via magnetospheric precipitation.

The origin and significance of these unusual features is currently subject to speculation. The similarity in coloration with, and magnetic conjugacy to, other overlying green features suggests a common optical spectrum dominated by the oxygen 557.7-nm emission. The point-like nature of the emission suggests excitation via turbulent electron heating, rather than variations in neutral oxygen density. Prior work on radar backscattered from ionospheric regions impinged by extreme electric fields has implicated an interplay among Farley-Buneman, ion-thermal, electron-thermal, and gradient-drift instabilities in creating small-scale irregularities in density and temperature in the lower ionospheric E-region (Dimant & Oppenheim, 2011). The evidence in these studies has been derived from radar backscatter and in situ plasma measurements. The extreme electric fields, and attendant extreme velocities, observed within STEVE have not been fully treated in theoretical or simulation studies. The question is whether under extreme conditions such mechanisms could produce an electron population exceeding the 4.19-eV threshold for green-line excitation, creating an observable optical diagnostic while also providing a mechanism to explain the point-source nature of these objects.

5 Next Steps

STEVE has elevated the role of citizen scientists in primary research. In their quest to obtain beautiful imagery of the natural world, photographers have serendipitously discovered a phenomenon overlooked by professional scientists. References to the optical phenomena of STEVE have since been uncovered in historical literature (Hunnekuhl & MacDonald, 2020), but without its current appreciation as a phenomenon distinct from the typical aurora and airglow (Gallardo-Lacourt, Liang, Nishimura, & Donovan, 2018).

Specific gaps in our understanding of STEVE can be filled through enhanced partnerships with citizen science community. First, we cannot yet state with certainty that the optical spectra of all green features are the same. Needed are collaborative observations from high frame-rate broad-band cameras of the type employed herein, and high resolution imaging spectrographs of the type employed by (Gillies et al., 2019). Second, there is a need for higher-cadence observations; the 3.5-second cadence of the image sequences used herein (figure 6) have not fully resolved STEVE phenomena. Third, carefully coordinated multi-site measurements are needed for better triangulation of orientations and trajectories of these features. This requires that precise geolocation and timing information be recorded into image metadata. And fourth, continued documenta-

tion and sharing of observations with the global community is needed – e.g., through the Aurorasaurus project (MacDonald et al., 2015)

Progress will also requires new collaborations within the Heliophysics community. If the fine-scale features described herein are a consequence of extreme electric fields, then they present a new diagnostic for understanding ionospheric instabilities and turbulence. Developing this capability requires that we fill the gap between theoretical predictions of heating rates to structured excitation of the 4.19-eV $O(^1S)$ state producing the visible features. This will require collaborative efforts that conjoin regional transport modeling (e.g., Zettergren & Semeter, 2012), kinetic plasma simulation (e.g., Oppenheim & Dimant, 2004), and aeronomical modeling of optical emissions (e.g., Solomon, 2017).

6 Acknowledgements

This work was supported by NASA under grant 80NSSC18K0659, and by the NSF under grant AGS-1821135. The authors are grateful to Steven Voss (Aurora Australis Facebook group), Shawn Malone (Great Lakes Photography) and Alan Dyer (www.amazingsky.com) for providing additional critical photographic evidence for this work. The figures presented herein, along with the supplemental videos, constitute the entirety of the new data in this work.

References

Anderson, P. C., Heelis, R. A., & Hanson, W. B. (1991, Apr). The ionospheric signatures of rapid subauroral ion drifts. *Journal of Geophysical Research*, *96*(A4), 5785-5792. doi: 10.1029/90JA02651

Archer, W. E., Gallardo-Lacourt, B., Perry, G. W., St.-Maurice, J. P., Buchert, S. C., & Donovan, E. (2019). Steve: The optical signature of intense subauroral ion drifts. *Geophysical Research Letters*, *46*(12), 6279-6286. doi: 10.1029/2019GL082687

Archer, W. E., St. -Maurice, J. P., Gallardo-Lacourt, B., Perry, G. W., Cully, C. M., Donovan, E., ... Eurich, D. (2019, Oct). The Vertical Distribution of the Optical Emissions of a Steve and Picket Fence Event. *Geophysical Research Letters*, *46*(19), 10,719-10,725. doi: 10.1029/2019GL084473

Bahcivan, H., & Cosgrove, R. (2010). On the generation of large wave parallel electric fields responsible for electron heating in the high-latitude e region. *Journal*

of Geophysical Research: Space Physics, *115*(A10). Retrieved from https://agupubs.onlinelibrary.wiley.com/doi/abs/10.1029/2010JA015424 doi: 10.1029/2010JA015424

Bates, D. R. (1993, Oct). Cause of Terrestrial Nightglow Continuum. *Proceedings of the Royal Society of London Series A*, *443*(1917), 227-237. doi: 10.1098/rspa.1993.0141

Dahlgren, H., Semeter, J. L., Marshall, R. A., & Zettergren, M. (2013, July). The optical manifestation of dispersive field-aligned bursts in auroral breakup arcs. *Journal of Geophysical Research*, *118*, 4572-4582. doi: 10.1002/jgra.50415

Dimant, Y., & Oppenheim, M. (2004). Ion thermal effects on e-region instabilities: linear theory. *Journal of Atmospheric and Solar-Terrestrial Physics*, *66*(17), 1639 - 1654. (40 Years of Equatorial Aeronomy Sparked by the Jicamarca Radio Observatory)

Dimant, Y., & Sudan, R. N. (1997). Physical nature of a new cross-field current-driven instability in the lower ionosphere. *Journal of Geophysical Research: Space Physics*, *102*(A2), 2551-2563. Retrieved from https://agupubs.onlinelibrary.wiley.com/doi/abs/10.1029/96JA03274 doi: 10.1029/96JA03274

Dimant, Y. S., & Oppenheim, M. M. (2011, September). Magnetosphere-ionosphere coupling through E region turbulence: 2. Anomalous conductivities and frictional heating. *Journal of Geophysical Research (Space Physics)*, *116*, A09304. doi: 10.1029/2011JA016649

Farley, D. T., Jr. (1963, November). A Plasma Instability Resulting in Field-Aligned Irregularities in the Ionosphere. *Journal of Geophysical Research*, *68*, 6083. doi: 10.1029/JZ068i022p06083

Fejer, B. G., & Kelley, M. C. (1980). Ionospheric irregularities. *Reviews of Geophysics*, *18*(2), 401–454. Retrieved from http://dx.doi.org/10.1029/RG018i002p00401 doi: 10.1029/RG018i002p00401

Foster, J. C., & Erickson, P. J. (2000). Simultaneous observations of e-region coherent backscatter and electric field amplitude at f-region heights with the millstone hill uhf radar. *Geophysical Research Letters*, *27*(19), 3177-3180. doi: 10.1029/2000GL000042

Gallardo-Lacourt, B., Liang, J., Nishimura, Y., & Donovan, E. (2018, Aug). On the

Origin of STEVE: Particle Precipitation or Ionospheric Skyglow? *Geophysical Research Letters*, *45*(16), 7968-7973. doi: 10.1029/2018GL078509

Gillies, D. M., Donovan, E., Hampton, D., Liang, J., Connors, M., Nishimura, Y., ... Spanswick, E. (2019, Jul). First Observations From the TREx Spectrograph: The Optical Spectrum of STEVE and the Picket Fence Phenomena. *Geophysical Research Letters*, *46*(13), 7207-7213. doi: 10.1029/2019GL083272

Haerendel, G., & Lüst, R. (1968, nov). Artificial Plasma Clouds in Space. *Scientific American*, *219*(5), 80-92. doi: 10.1038/scientificamerican1168-80

Haldoupis, C., Ogawa, T., Schlegel, K., Koehler, J. A., & Ono, T. (2005, November). Is there a plasma density gradient role on the generation of short-scale Farley-Buneman waves? *Annales Geophysicae*, *23*(10), 3323-3337. doi: 10.5194/angeo-23-3323-2005

Harding, B. J., Mende, S. B., Triplett, C. C., & Wu, Y.-J. J. (2020). A mechanism for the steve continuum emission. *Geophysical Research Letters*, *47*(7), e2020GL087102. Retrieved from `https://agupubs.onlinelibrary.wiley.com/doi/abs/10.1029/2020GL087102` (e2020GL087102 2020GL087102) doi: 10.1029/2020GL087102

Hunnekuhl, M., & MacDonald, E. (2020). Early Ground-Based Work by Auroral Pioneer Carl Stormer on the High-Altitude Detached Subauroral Arcs Now Known as "STEVE". *Space Weather*, *18*(3), e2019SW002384. Retrieved from `https://agupubs.onlinelibrary.wiley.com/doi/abs/10.1029/2019SW002384` doi: 10.1029/2019SW002384

Itikawa, Y., & Ichimura, A. (1990, May). Cross Sections for Collisions of Electrons and Photons with Atomic Oxygen. *Journal of Physical and Chemical Reference Data*, *19*(3), 637-651. doi: 10.1063/1.555857

Lang, D., Hogg, D. W., Mierle, K., Blanton, M., & Roweis, S. (2010). Astrometry.net: Blind astrometric calibration of arbitrary astronomical images. *AJ*, *137*, 1782–2800. (arXiv:0910.2233)

Liang, J., Donovan, E., Connors, M., Gillies, D., St-Maurice, J. P., Jackel, B., ... Chu, X. (2019, December). Optical Spectra and Emission Altitudes of Double-Layer STEVE: A Case Study. *Geophysical Research Letters*, *46*(23), 13,630-13,639. doi: 10.1029/2019GL085639

Linson, L. M., & Workman, J. B. (1970). Formation of striations in ionospheric

plasma clouds. *Journal of Geophysical Research (1896-1977)*, *75*(16), 3211-3219. Retrieved from https://agupubs.onlinelibrary.wiley.com/doi/abs/10.1029/JA075i016p03211 doi: 10.1029/JA075i016p03211

MacDonald, E. A., Case, N. A., Clayton, J. H., Hall, M. K., Heavner, M., Lalone, N., ... Tapia, A. (2015, 9). Aurorasaurus: A citizen science platform for viewing and reporting the aurora. *Space Weather*, *13*(9), 548–559. Retrieved from http://doi.wiley.com/10.1002/2015SW001214 doi: 10.1002/2015SW001214

MacDonald, E. A., Donovan, E., Nishimura, Y., Case, N. A., Gillies, D. M., Gallardo-Lacourt, B., ... Schofield, I. (2018, Mar). New science in plain sight: Citizen scientists lead to the discovery of optical structure in the upper atmosphere. *Science Advances*, *4*(3). doi: 10.1126/sciadv.aaq0030

Meeus, J. (1991). *Astronomical algorithms*. Willmann-Bell.

Mende, S. B., Harding, B. J., & Turner, C. (2019, December). Subauroral Green STEVE Arcs: Evidence for Low-Energy Excitation. *Geophysical Research Letters*, *46*(24), 14,256-14,262. doi: 10.1029/2019GL086145

Mishin, E., & Streltsov, A. (2019). Steve and the picket fence: Evidence of feedback-unstable magnetosphere-ionosphere interaction. *Geophysical Research Letters*, *46*(24), 14247-14255. doi: 10.1029/2019GL085446

Nishimura, Y., Bortnik, J., Li, W., Thorne, R. M., Lyons, L. R., Angelopoulos, V., ... Auster, U. (2010, October). Identifying the Driver of Pulsating Aurora. *Science*, *330*, 81. doi: 10.1126/science.1193186

Nishimura, Y., Gallardo-Lacourt, B., Zou, Y., Mishin, E., Knudsen, D. J., Donovan, E. F., ... Raybell, R. (2019, Jun). Magnetospheric Signatures of STEVE: Implications for the Magnetospheric Energy Source and Interhemispheric Conjugacy. *Geophysical Research Letters*, *46*(11), 5637-5644. doi: 10.1029/2019GL082460

Oppenheim, M. M., & Dimant, Y. S. (2004, November). Ion thermal effects on E-region instabilities: 2D kinetic simulations. *Journal of Atmospheric and Solar-Terrestrial Physics*, *66*(17), 1655-1668. doi: 10.1016/j.jastp.2004.07.007

Oppenheim, M. M., & Dimant, Y. S. (2013). Kinetic simulations of 3-d farley-buneman turbulence and anomalous electron heating. *Journal of Geophysical Research: Space Physics*, *118*(3), 1306-1318. doi: 10.1002/jgra.50196

Rishbeth, H., & Garriott, O. (1969). *Introduction to ionospheric physcis*. Academic Press.

Simons, D. J., Pongratz, M. B., & Gary, S. P. (1980, Feb). Prompt striations in ionospheric barium clouds due to a velocity space instability. *Journal of Geophysical Research*, *85*(A2), 671-677. doi: 10.1029/JA085iA02p00671

Solomon, S. C. (2017). Global modeling of thermospheric airglow in the far ultraviolet. *Journal of Geophysical Research: Space Physics*, *122*(7), 7834-7848. doi: 10.1002/2017JA024314

Streltsov, A. V., & Mishin, E. V. (2003). Numerical modeling of localized electromagnetic waves in the nightside subauroral zone. *Journal of Geophysical Research: Space Physics*, *108*(A8). doi: 10.1029/2003JA009858

Thébault, E., Finlay, C. C., Beggan, C. D., Alken, P., Aubert, J., Barrois, O., ... Zvereva, T. (2015). International geomagnetic reference field: The 12th generation international geomagnetic reference field - The twelfth generation. *Earth, Planets and Space*, *67*(1). doi: 10.1186/s40623-015-0228-9

Vincenty, T. (1975). Direct and inverse solutions of geodesics on the ellipsoid with application of nested equations. *Survey Review*, *23*(176), 88-93. doi: 10.1179/sre.1975.23.176.88

Zettergren, M., & Semeter, J. (2012). Ionospheric plasma transport and loss in auroral downward current regions. *Journal of Geophysical Research: Space Physics*, *117*(A6). doi: 10.1029/2012JA017637